Available online at www.sciencedirect.com

ScienceDirect

Journal of the European Ceramic Society 31 (2011) 61–74

www.elsevier.com/locate/jeurceramsoc

MgO–$CaZrO_3$-based refractories for cement kilns

Álvaro Obregón [a,b], Jose Luis Rodríguez-Galicia [b], Jorge López-Cuevas [b], Pilar Pena [a], Carmen Baudín [a,*]

[a] *Instituto de Cerámica y Vidrio, CSIC, Kelsen 5, 28049 Madrid, Spain*
[b] *CINVESTAV, Unidad Saltillo, Coahuila, 25000 Saltillo, Mexico*

Received 1 July 2010; received in revised form 27 July 2010; accepted 25 August 2010

Abstract

Two series of refractory materials have been designed taking into account the phase equilibrium relationships to obtain MgO–$CaZrO_3$–Ca_2SiO_4–$Ca_3Mg(SiO_4)_2$ or MgO–$CaZrO_3$–$Ca_3Mg(SiO_4)_2$–c-ZrO_2 as final crystalline phases. Specimens have been fabricated by reaction sintering of natural dolomite and zircon and with dead burned magnesia aggregates. Different relationships between the proportion and sizes of the fines and the aggregates have been explored.

The microstructure of the materials has been characterized in terms of density, crystalline phases and phase distribution and morphology. A combination of X-ray diffraction (XRD) analyses and reflected light optical microscopy and scanning electron microscopy with microanalysis have been used. The phases present in the materials are those expected from the phase equilibrium relationships in the quaternary system. The optimum microstructures, i.e. minimum porosity and adequate matrix content to constitute the bonding between the aggregates are found for initial matrix fractions higher than those for non-reactive systems.

The mechanical behaviour has been determined in terms of the room temperature dynamic Young's modulus, E, and the three point bending modulus of rupture, MOR, at 25 and 1100 °C. Additionally, the work of fracture, WOF, has been calculated from the load–displacement curves of stable fracture tests.

For optimum starting mixtures, materials with E (60–80 GPa), MOR (4–6 and ~10 MPa at 25 and 1100 °C, respectively) and WOF (40–70 J m^{-2}) values in the range of those of other magnesia-based refractories have been obtained.

Keywords: Powders—solid state reaction; Microstructure—final; Mechanical properties; MgO; Refractories

1. Introduction

Portland cements are constituted by mixtures of synthetic calcium silicates obtained from the reaction of natural raw materials. The major raw material is limestone ($CaCO_3$) whereas minor ones to be the silica (SiO_2) sources can be clay, sand, iron ore, shale, fly ashes and slags. The fabrication process of modern Portland cements involves firing at temperatures around 1500 °C in rotary kilns.[1] The final product is called clinker and is basically formed by four crystalline phases: alite (Ca_3SiO_5), belite (β-Ca_2SiO_4), tricalcium aluminate ($Ca_3Al_2O_6$) and ferrite ($Ca_2(Al_XFe_{2-X})_2O_5$); minor common components are Na_2SO_4, K_2SO_4, $CaSO_4$ and KCl. Therefore, the process involves aggressive basic environments and atmospheres with high alkali and sulphur contents that can strongly modify the microstructure and phase composition of the refractories of the work zone of the kilns.

Magnesia–chrome refractories (from silicate bonded to direct bond) have been used in rotary kilns for a long period because of their resistance to cement clinker attack due to their ability to develop protective coatings in the upper transition and burning zones. However, chrome-free lining of cement rotary kilns is one of the most important subjects in the refractory field from the view point of environmental protection due to the carcinogenic issues related to hexavalent chromium ($CrO_4{}^{2-}$). Refractory wastes with more than 5 mg/l of Cr are forbidden in European and USA legislations.[2,3] In order to substitute the chrome-based materials, refractories containing magnesia (MgO) aggregates and matrices of magnesia and magnesium–aluminium spinel ($MgAl_2O_4$) have been developed and used in the cement industry. Nevertheless, the composition of such materials is not an adequate one from the stand point of thermodynamics, as

---

[*] Corresponding author. Tel.: +34 917355840; fax: +34 917355843.
E-mail address: cbaudin@icv.csic.es (C. Baudín).

0955-2219/$ – see front matter © 2010 Elsevier Ltd. All rights reserved.
doi:10.1016/j.jeurceramsoc.2010.08.020

they would form liquids at low temperatures (≈1400 °C) when combined with the components of cement, as can be recognised from the phase equilibrium relationships in the system Al_2O_3–CaO–SiO_2–MgO.[4–6] In fact, magnesia-spinel refractories present relatively low corrosion resistance under the work conditions in the cement kilns.

As the fine grains that constitute the matrix of a refractory are much more reactive than the aggregates, a general rule for refractory design is that the matrix composition has to be more resistant to corrosion than that of the aggregates. In this sense, the studies of the melting and solid-state compatibility relationships in the system CaO–MgO–ZrO_2–SiO_2 have demonstrated that MgO–$CaZrO_3$-based refractories containing calcium silicates could be an alternative to the MgO–$MgAl_2O_4$ ones due to the high temperatures for liquid formation in the MgO–$CaZrO_3$-rich area of the MgO–CaO–ZrO_2–SiO_2 system (~1550 °C).[5,6]

In particular, calcium zirconate ($CaZrO_3$) is a phase with very high melting point (~2340 °C), without polymorphic transformations and which is compatible with MgO and with the main phases of Portland cement clinker (Ca_2SiO_4 and Ca_3SiO_5). Moreover, the solid–solid bonding between the compatible MgO and $CaZrO_3$ phases is highly resistant to the penetration of fluxes from the clinker, as has been demonstrated by corrosion studies using cement clinker with MgO and $CaZrO_3$-based fine grained materials.[7–10] MgO–$CaZrO_3$-based materials can be obtained by reaction sintering of natural raw materials such as dolomite ($MgCa(CO_3)_2$) and zircon ($ZrSiO_4$).[11–15]

$CaZrO_3$ presents a crystalline average thermal expansion coefficient (α average between 25 and 1000 °C, $\alpha_{25\text{–}1000\,°C} \approx 10.4 \times 10^{-6}\,°C^{-1}$)[16] lower than that of MgO ($\alpha_{25\text{–}1000\,°C} \approx 13.5 \times 10^{-6}\,°C^{-1}$)[17] and large thermal expansion anisotropy ($\alpha_a = 4.9 \times 10^{-6}\,°C^{-1}$, $\alpha_b = 10.9 \times 10^{-6}\,°C^{-1}$, $\alpha_c = 15.1 \times 10^{-6}\,°C^{-1}$). Therefore, residual stresses due to thermal expansion mismatch can be developed during cooling from the fabrication temperature at the boundaries between MgO and $CaZrO_3$ grains. The level and sign of the stresses will be determined by the relative orientation of grains. Moreover, residual stresses can also be developed inside the $CaZrO_3$ at the boundaries between crystallites with different orientations. Depending on the specific microstructure of the material, the residual stresses can lead to microcracking in the material during cooling from the sintering temperature or interact with external applied stresses. This interaction can cause decrease or increase of the effective stresses experienced by the piece at the microstructural scale and microcracking of the material prior to or during fracture. Therefore, an adequate microstructural design can lead to materials with improved mechanical behaviour.

Table 1
Properties of the MgO–$CaZrO_3$-additional phase dense composites previously studied [13].

Property	Additional phase	
	Ca_2SiO_4	$Ca_3Mg(SiO_4)_2$
Relative density (% of theoretical)	98 ± 1	96 ± 1
Average thermal expansion between 25 and 925 °C ($\times 10^{-6}\,°C^{-1}$)	12.8 ± 0.3	10.0 ± 0.4
Young's modulus (GPa)	194 ± 2	181 ± 2
Room temperature bend strength (MPa)	304 ± 24	118 ± 11
SENB toughness (4 point bending) ($MPa\,m^{-1/2}$)	2.1 ± 0.3	2.6 ± 0.2

In a previous work,[14] the reaction sintering of $MgCa(CO_3)_2$/$ZrSiO_4$ mixtures to obtain MgO–$CaZrO_3$–Ca_2SiO_4 and MgO–$CaZrO_3$–$Ca_3Mg(SiO_4)_2$ dense (>96% of theoretical) and fine grained (≈1–4 μm) materials was reported. The thermal expansion and the mechanical behaviour of the studied materials was that of materials made of a matrix of MgO–$CaZrO_3$ and with dispersed ternary phases with similar Young's modulus (116 and 130 GPa for $Ca_3Mg(SiO_4)_2$ and β-Ca_2SiO_4, respectively) and very different thermal expansion coefficients (7.5 and $16.3 \times 10^{-6}\,°C^{-1}$ for $Ca_3Mg(SiO_4)_2$ and β-Ca_2SiO_4, respectively). No microcracking was observed in the MgO–$CaZrO_3$–β-Ca_2SiO_4 material due to thermal expansion mismatch and it presented high strength values (304 ± 24 MPa) and brittle fracture mode. In contrast, the MgO–$CaZrO_3$–$Ca_3Mg(SiO_4)_2$ material developed microcracking during fracture with associated low strength (118 ± 11 MPa). In Tables 1 and 2,[14,17–22] the properties of both previously studied composites as well as those of their constituent phases are summarised.

In this work, the feasibility of extending the reaction sintering approach to obtain MgO–$CaZrO_3$-based or MgO-cubic ZrO_2 (c-ZrO_2) based basic refractories for cement kilns is studied. The proposed materials are constituted by periclase aggregates bonded by matrices of MgO–$Ca_3Mg(SiO_4)_2$–$CaZrO_3$ or MgO–$Ca_3Mg(SiO_4)_2$–c-ZrO_2 with Ca_2SiO_4 or $CaZrO_3$ as additional phases. The processing as well as the microstructure and the mechanical behaviour of the materials are described.

Table 2
Properties of the phases present in the green bodies and the expected constituent phases of the sintered materials. *E*: determined for monophase and dense materials.

	$CaMg(CO_3)_2$	$ZrSiO_4$	MgO	$CaZrO_3$	β-Ca_2SiO_4	c-$ZrO_2Ca_{0.5}Zr_{0.85}O_{1.85}$	$Ca_3Mg(SiO_4)_2$
Theoretical density (g/cm^3)	2.863	4.669	3.585	4.619	3.313	5.269	3.312
ASTM XRD file	36-426	6-226	45-946	35-790	33-0302	1-084-1829	35-0591
Young's modulus (GPa)			≈270[17]	≈231[18]	≈130[a]	218±3[19]	≈116[13]
$\alpha_{25\text{–}1000} \times 10^{-6}\,°C^{-1}$			≈13.5[20]	≈10.4[15]	≈16.3[21]	≈10[22]	7.4[b]

[a] Extrapolated for monophase Ca_2SiO_4 from data in Ref. [18].

[b] Calculated in Ref. [13].

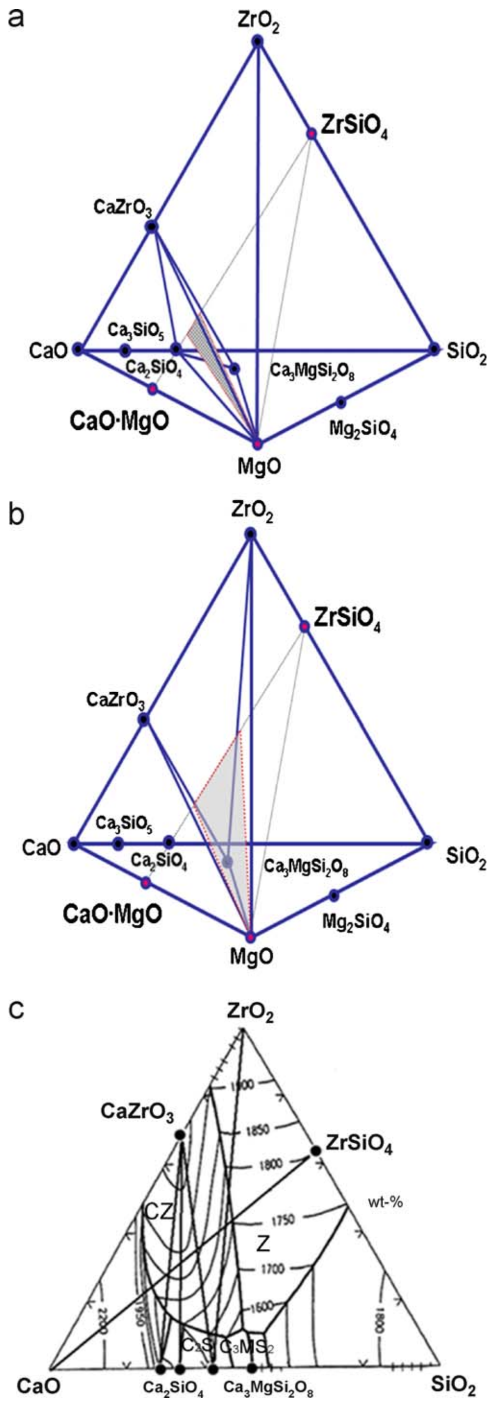

Fig. 1. Diagrammatic representations of the solid state phase equilibrium relationships in the quaternary system MgO–CaO–SiO_2–ZrO_2 used for the formulation of the matrices of the materials. The final compositions of the materials are summarised in Table 5. (a) Matrices MII formulated according to Eq. (1). These matrices were used to fabricate materials RII. (b) Matrices MIII formulated according to Eq. (2). These matrices were used to fabricate materials RIII. (c) Projection from the MgO–apex on the opposite face of the quaternary tetrahedron (triangle CaO–ZrO_2–SiO_2) showing the secondary phases and the invariant points for the MgO–CaO–ZrO_2–SiO_2 mixtures CZ = $CaZrO_3$, Z = ZrO_2, C_2S = Ca_2SiO_4, C_3MS_2 = $Ca_3Mg(SiO_4)_2$.

The matrix of the refractories was formulated on the basis of the information supplied by the system CaO–MgO–ZrO_2–SiO_2.[5,6] In Fig. 1a and b the diagrammatic representations of the solid state relationships used for the formulation of the matrices of the materials are shown, in Fig. 1c the secondary phases and the invariant points are represented.

All studied matrices lie in the connecting line $ZrSiO_4$–$MgCa(CO_3)_2$. The compositions MII (Fig. 1a) designed according to Eq. (1):

$$(1+x)\mathrm{ZrSiO_4} + (3+2x)\mathrm{CaMg(CO_3)_2} \rightarrow (3+x)\mathrm{MgO} + (1+x)\mathrm{CaZrO_3} + (1-x)\mathrm{Ca_2SiO_4} + (x)\mathrm{Ca_3Mg(SiO_4)_2} + (6+4x)\mathrm{CO_2} \quad (1)$$

are located in the solid-state compatibility tetrahedron MgO–$CaZrO_3$–Ca_2SiO_4–$Ca_3Mg(SiO_4)_2$, for which the invariant point is 1550 °C (Fig. 1c). For the composition with only MgO, $CaZrO_3$, and Ca_2SiO_4 ($x = 0$) the temperature for first liquid formation will be between this temperature and that of the invariant point of the compatibility tetrahedron MgO–$CaZrO_3$–Ca_2SiO_4 –Ca_3SiO_5 (1710 °C, Fig. 1c).

The MII matrices would contain similar amounts of MgO + $CaZrO_3$ (55–58 vol.%), and would differ in the nature of the silicate phase, β-Ca_2SiO_4 and/or $Ca_3Mg(SiO_4)_2$, according to the stoichiometry of the starting mixture.

The compositions MIII (Fig. 1b), designed according to Eq. (2):

$$2\mathrm{ZrSiO_4} + (5-2x)\mathrm{CaMg(CO_3)_2} \rightarrow (4-2x)\mathrm{MgO} + 2(1-x)\mathrm{CaZrO_3} + (2x)\mathrm{ZrO_2} + \mathrm{Ca_3Mg(SiO_4)_2} + (10-4x)\mathrm{CO_2} \quad (2)$$

are located in the solid-state compatibility tetrahedron MgO–$CaZrO_3$–$Ca_3Mg(SiO_4)_2$–ZrO_2, for which the invariant point is 1475 °C (Fig. 1c). The composition with $x = 0$ coincides with MII with $x = 1$ (Eqs. (1) and (2)) and the composition with $x = 1$ is a ternary one constituted by MgO–ZrO_2–$Ca_3Mg(SiO_4)_2$ for which the temperature for first liquid formation is 1470 °C (Fig. 1c).

As the temperatures for first liquid formation in matrices MIII would be lower than those corresponding to the matrices MII, the sintering temperatures chosen for the compacts with composition according to Eq. (2) were lower than those for the ones formulated according to Eq. (1).

The actual temperatures for liquid formation in the real materials will be lower than the above discussed ones due to the presence of small amounts of impurities in the natural raw materials.

The compositions of the initial mixtures used to fabricate the actual materials, formed by mixing the fine grained (<120 μm) $ZrSiO_4$–$MgCa(CO_3)_2$ mixtures with the MgO aggregates (0.21–3.3 mm), are located in the formulation triangle $ZrSiO_4$–$MgCa(CO_3)_2$–MgO (Fig. 1).

The adequate mixtures of MgO particles with different size distributions for optimum packing in the green compacts have been calculated using the approach by Funk and Dinger[23] which is a modification of the classical Andreasen distribution to include minimum particle sizes different from zero. For these authors:

$$\frac{\text{CPTF}}{100} = \frac{(D^m - D_S^m)}{(D_L^m - D_S^m)} \tag{3}$$

where CPFT = Cumulative Percent (of particles) Finer Than (i.e. with diameter smaller than D); D = particle diameter; D_L = the largest particle size; D_S = smallest particle size; m = the distribution modulus.

Densest packing of the particles would occur for distribution modulus equal to 0.37.

In principle, optimum packing in the green compacts will lead to sintered materials with minimum and homogeneously distributed porosity. Nevertheless, as the matrices of the green compacts with the compositions studied here will experience extreme volume changes from relatively low temperatures (∼600–800 °C) due to decarbonation of $MgCa(CO_3)_2$ the results obtained for non-reacting systems might not be valid. Moreover, the composition of the materials will be the result of the high temperature reactions between the initial constituents. Therefore, three different modules (0.15, 0.37 and 0.45) have been used for the granulometric design.

2. Experimental

2.1. Fabrication of materials

The raw materials used were natural zircon mineral (American Minerals, Smurfit-Stone, USA), a natural polycrystalline dolomite (Peñoles; Química del Rey, Cohauila, Mexico) and synthetic periclase aggregates (Magnelec; Ramos Arizpe, Coahuila, Mexico). The periclase had three size fractions ranging from 600 μm to 3.35 mm, 425 μm to 1.7 mm and 210 μm to 1 mm. The zircon mineral had an initial particle size of 3000 μm and was previously milled for 2 h using MgO balls down to 60 μm in batches of 2 kg to reach a total amount of 10 kg. The dolomite had an average particle size around 40 μm.

Chemical analyses of the three raw materials were carried out by inductively coupled plasma (ICP) and X-ray fluorescence spectroscopy (XRF, Magi X; Phillips, the Netherlands) and flame emission spectrometry for alkaline analyses (Na and K) (FES, 2100; Perkin Elmer, USA).

The processing route followed to produce the refractory materials included the following steps: (a) conditioning the raw materials, (b) attrition milling of the dolomite–zircon mixtures to constitute the matrix, with MgO-partially stabilized zirconia balls, in water media, for 4 h, (c) homogenizing of the mixtures of milled zircon–dolomite mixtures and the three types of periclase aggregates by ball milling using MgO balls for 1 h in water, (d) uniaxial pressing at 300 MPa (Enerpac PE S1201B, WI, USA) for 5 min into cylinders (25 mm diameter, 57 mm height) using stainless steel moulds, (e) firing in an electrical furnace (46240 Thermolyne, TX, USA) using 2 °C/min as heating and cooling rates and 6 h as holding time at the maximum temperature (in the range 1450–1650 °C, depending on the composition, Table 4). For the thermal treatments the specimens were placed on alumina supports covered by Y_2O_3 stabilized zirconia balls.

2.2. Characterization

Different specimens were machined from the sintered cylinders using diamond disks for characterization. Additionally, relatively large (∼150 mm × 25 mm × 25 mm) specimens were ground in a tungsten carbide ball mill and the portions to be analysed were extracted from the ground powders in order to have a representative portion of the materials.

The crystalline phases present in the sintered materials were analysed by X-ray powder diffraction (XRD). The XRD patterns were recorded with a graphite monochromated Cu K_α radiation in a Kristalloflex D5000 (Siemens, Germany) diffractometer (Bragg–Brentano geometry) working at 40 kV and 30 mA. Data collection was taken on samples rotating at 15 rpm in the interval 10–70° (in 2θ).

The XRD diffractograms were analysed using the ASTM files 45-946, 35-790, 33-0302, 1-084-1829 and 35-0591, for MgO, $CaZrO_3$, β-Ca_2SiO_4, CaO stabilized cubic zirconia, c-ZrO_2 ($Ca_{0.5}Zr_{0.85}O_{1.85}$) and $Ca_3Mg(SiO_4)_2$, respectively.

The apparent density of five specimens (∼40 mm × 25 mm × 25 mm) was determined following the procedure of the EN993-1 standard and the true density was determined by helium pycnometry (Multipycnometer Quantachrome, FL, USA) using five different portions extracted from the previously milled powder. The total porosity was calculated from the apparent and real density values. Reported values are the average of the five determinations and errors are the standard deviations.

The microstructure was observed by reflected light optical microscopy (RLOM; Zeiss Oberkochen, Germany) and scanning electron microscopy with dispersive X-ray energy (SEM-EDX, Philips XL30 ESEM, The Netherlands) on samples polished to a mirror finish using 6, 3 and 1 μm diamond suspensions.

Mechanical characterization has been done, using specimens of 150 mm × 25 mm × 25 mm, in terms of Young's modulus, modulus of rupture (MOR) and work of fracture (WOF) for each material. Dynamic Young's modulus was calculated from the resonance frequency (Grindosonic, Belgium) of bars tested by impact in flexure; reported values are the average of the 10 determinations and errors are the standard deviations. Room temperature modulus of rupture was determined by three point bending (span 150 mm) following the procedure of EN993-6 standard, using a universal testing machine (Microtest, Spain) with stainless steel supports; reported values are the average of seven determinations and errors are the standard deviations. Bending tests at 1100 °C were performed in a specially developed mechanical testing device with high purity dense alumina supports[24] using the same loading conditions as for the room temperature tests (EN993-7). Six specimens randomly selected from the different materials were tested in a single thermal cycle; heating rate was 5 °C/min and holding times before testing ranged from 20 to 60 min. Reported values are the average of three determinations and errors are the standard deviations.

The load–displacement curves were recorded during the bending tests and the WOF was calculated as the area under the curves divided by twice the cross section of the specimens.

Table 3
Composition of the matrices and corresponding calculated theoretical weight losses due to the presence of carbonates.

Material		Green body					Sintered materials	
Composition	Modulus	Matrix (wt.%)			Matrix proportion in the material		Total loss wt.% CO_2	Matrix (vol.%)
		Dolomite	Zircon	CO_2	vol.%	wt.%		
RII $x = 0$	0.15	73	27	35	58.7	60.2	21.1	49
	0.37				39.6	41.1	14.4	31
	0.45				33.9	35.3	12.4	26
RII $x = 0.5$	0.15	71	29	33	47.1	48.8	16.1	39
	0.37				31.0	32.5	10.7	24
	0.45				26.4	27.7	9.1	20
RII $x = 1$	0.15	69	31	33	50.3	51.2	16.9	41
	0.37				32.7	34.3	11.3	26
	0.45				27.9	29.3	9.7	22
RIII $x = 0.5$	0.15	65	35	31	48.2	50.2	15.6	41
	0.37				31.9	33.6	10.4	26
	0.45				27.1	28.7	8.9	22
RIII $x = 1$	0.15	59	41	28	48.7	51.7	14.5	43
	0.37				32.9	34.9	9.8	28
	0.45				28.0	29.8	8.3	23

Only the curves showing stable or semi-stable fracture were used for WOF determinations.

3. Results and discussion

3.1. Chemical composition of the raw materials

The chemical analyses of dolomite indicated that its composition (wt.%) was: 32.27% CaO, 20.01% MgO, 0. 14% Al_2O_3, 0.12% SiO_2, 0.003% P_2O_5, 0.084% SO_3, 0.013% K_2O, 0.012% MnO_2, 0.13 Fe_2O_3 and 0.01% SrO, with a loss ignition of 47.2% at 900 °C; contrary to other dolomite minerals reported in the literature it contained very small amounts of iron and/or manganese.

XRD analyses indicated that the powder major constituent was $CaMg(CO_3)_2$ and that it contained a small amount of $CaCO_3$ (≈3 wt.%), in agreement with the chemical analyses. Rational analysis using the chemical composition determined for the dolomite indicated that the amounts of the crystalline phases were (in wt.%): ≈96 of $CaMg(CO_3)_2$, 3% of $CaCO_3$ and 0.5% of other inorganic constituents.

The chemical composition of zircon (in wt.%) was: 0.21% CaO, 0.035% MgO, 0.61% Al_2O_3, 31.17% SiO_2, 0.005% K_2O, 0.018% Na_2O, 67.84% $ZrO_2 + Hf_2O$ and 0.12 Fe_2O_3. This chemical composition is very close to the stoichiometric composition of $ZrSiO_4$, the only crystalline phase detected by XRD.

The periclase (MgO) aggregates were highly pure, with chemical composition (in wt.%): 99.13% MgO, 0.633% CaO, <0.006% Al_2O_3, 0.160% SiO_2, 0.010% MnO_2, 0.001% ZrO_2 and 0.066 Fe_2O_3 ($CaO/SiO_2 > 4.2$ mol).

From the chemical analyses of the raw materials, the total amount of impurities in the studied materials (∼1 wt.%) will be significant in lowering the temperatures for first liquid formation.

3.2. Thermal behaviour of compositions

According to previous studies[25,14,15] in specimens with composition similar to those used here ($MgO–ZrSiO_4–CaMg(CO_3)_2$ mixtures), the reaction sintering process occurs in two well separated phenomena: first reaction and then porosity removal. Moreover, the dolomite mineral used decomposes in two well defined steps, both accompanied by a release of gaseous CO_2. The decomposition of $MgCa(CO_3)_2$ takes place at ∼775 °C yielding $CaCO_3$ and MgO while the decomposition of $CaCO_3$ occurs at ∼870 °C. Therefore, the matrices of the green compacts studied would experience very high weight losses during the thermal treatment from relatively low temperatures (≤1200 °C). Table 3 shows the expected weight losses calculated for the different compositions (28–35% wt.% of CO_2); these high weight losses will lead to porosity increases in the bodies before the occurrence of the sintering process.

As discussed in Section 1, the considered compositions are located in different compatibility volumes with different invariant points. Stable liquids are expected to form at temperatures ranging from 1450 to 1775 °C depending on the composition (Fig. 1 and Table 4).

3.3. Crystalline phases formed in the materials

In Table 4 the crystalline phases identified by XRD in the sintered materials are summarised and Table 5 shows the expected mineralogical composition calculated by rational analysis taking into account the formulation of the compositions (Eqs. (1)–(4)), the chemical analyses of the raw materials and the phase equilibrium diagram $ZrO_2–CaO–MgO–SiO_2$ (Fig. 1). The XRD results agreed with the calculated compositions.

Table 4
Expected and experimental crystalline phases in the materials.

Composition	*m*	Expected phases/ invariant point[4,5]	Sintering temperature (°C)	Phases identified by XRD			
				Major phase	Significant	Minor	Traces
RII $x = 0$	0.15	MgO–$CaZrO_3$–Ca_2SiO_4 1710 °C	1650	MgO	$CaZrO_3$	$Ca_3Mg(SiO_4)_2$	Ca_2SiO_4
	0.37			MgO	$CaZrO_3$	Ca_2SiO_4,$Ca_3Mg(SiO_4)_2$	
	0.45			MgO	$CaZrO_3$	Ca_2SiO_4, $Ca_3Mg(SiO_4)_2$	
RIII $x = 0.5$	0.15	MgO–$CaZrO_3$–Ca_2SiO_4–$Ca_3Mg(SiO_4)_2$ 1550 °C	1600	MgO	$CaZrO_3$	$Ca_3Mg(SiO_4)_2$, Ca_2SiO_4	
	0.37			MgO	$CaZrO_3$	$Ca_3Mg(SiO_4)_2$, Ca_2SiO_4	
	0.45			MgO	$CaZrO_3$	$Ca_3Mg(SiO_4)_2$, Ca_2SiO_4	
RII $x = 1$	0.15	MgO–$CaZrO_3$–$Ca_3Mg(SiO_4)_2$ 1475 °C < T_i < 1555 °C	1550	MgO	$Ca_3Mg(SiO_4)_2$, CaZrO3		c-ZrO_2
	0.37			MgO	$Ca_3Mg(SiO_4)_2$, $CaZrO_3$		c-ZrO_2
	0.45			MgO	$Ca_3Mg(SiO_4)_2$, $CaZrO_3$	c-ZrO_2	
RIII $x = 0.5$	0.15	MgO–$CaZrO_3$–ZrO_2–$Ca_3Mg(SiO_4)_2$ 1475 °C	1500	MgO	$CaZrO_3$, c-ZrO_2	$Ca_3Mg(SiO_4)_2$	
	0.37			MgO	$CaZrO_3$, c-ZrO_2	$Ca_3Mg(SiO_4)_2$	
	0.45			MgO	$CaZrO_3$, c-ZrO_2	$Ca_3Mg(SiO_4)_2$	
RIII $x = 1$	0.15	MgO-ZrO_2-$Ca_3Mg(SiO_4)_2$ 1470 °C	1450	MgO	c-ZrO_2	$Ca_3Mg(SiO_4)_2$	$CaZrO_3$
	0.37			MgO	c-ZrO_2	$Ca_3Mg(SiO_4)_2$	$CaZrO_3$
	0.45			MgO	c-ZrO_2	$Ca_3Mg(SiO_4)_2$	$CaZrO_3$

Table 5
Calculated volume fractions of the crystalline phases expected in the materials.

Composition	*m*	$CaZrO_3$	c-ZrO_2	Ca_2SiO_4	Ca_3MgSiO_4	MgO
RII $x = 0$	0.15	0.20	0.00	0.25	0.00	0.55
	0.37	0.13	0.00	0.17	0.00	0.70
	0.45	0.11	0.00	0.14	0.00	0.74
RII $x = 0.5$	0.15	0.17	0.00	0.04	0.16	0.62
	0.37	0.11	0.00	0.03	0.11	0.75
	0.45	0.10	0.00	0.02	0.09	0.79
RII $x = 1$	0.15	0.19	0.00	0.00	0.23	0.58
	0.37	0.12	0.00	0.00	0.15	0.73
	0.45	0.10	0.00	0.00	0.13	0.77
RIII $x = 0.5$	0.15	0.11	0.06	0.00	0.25	0.59
	0.37	0.07	0.04	0.00	0.16	0.73
	0.45	0.06	0.03	0.00	0.14	0.77
RIII $x = 1$	0.15	0.01	0.13	0.00	0.29	0.57
	0.37	0.01	0.09	0.00	0.19	0.71
	0.45	0.01	0.08	0.00	0.17	0.75

For compositions RII the main phases present in the samples were MgO and $CaZrO_3$; $Ca_3Mg(SiO_4)_2$ (merwinite) and Ca_2SiO_4 were present in smaller amounts which depended on the specific material.

MgO, $CaZrO_3$ and $Ca_3Mg(SiO_4)_2$ were also present in the RIII specimens. However, while MgO was the major phase as in materials RII, the relative intensity of the XRD peaks corresponding to $CaZrO_3$ decreased gradually from RII $x = 0$ to RIII $x = 1$, qualitatively indicating that the latter composition contained smaller amounts of this phase. The disappearance of $CaZrO_3$ from RIII $x = 0$ to RIII $x = 1$ was accompanied with the simultaneous appearance of c-ZrO_2; Ca_2SiO_4 was not detected in this group of samples.

3.4. Microstructural characterization

In Table 6 the values of density and porosity of the studied materials are summarised and Figs. 2–6 show characteristic microstructures. The theoretical density values were calculated using the theoretical densities of the present phases from the ASTM files (Table 2) and the calculated expected compositions (Table 5).

In most cases, differences between the porosities of the green and the sintered bodies as a function of the distribution modulus, *m*, were not significant. Moreover, the two materials that presented the lowest green porosities (RII $x = 0.5$, $m = 0.15$ and RIII $x = 1$, $m = 0.15$, Table 6) did not have the corresponding lowest sintered porosities. In addition, the sintered material RIII $x = 0.5$, $m = 0.15$ had the lowest porosity while the green porosity was similar to those of the other materials. The final materials were the result of the high temperature reactions between the initial constituents; therefore, as discussed in Section 1, optimum packing in the green compacts did not lead to sintered materials with minimum and homogeneously distributed porosity.

The macrostructure of the materials (Figs. 2–5) was composed of homogeneous distributions of aggregates of MgO (0.1–3.5 mm, 77–51 wt.%, from Table 3), fine fractions or matri-

Table 6
Density and porosity values of the materials.

Composition	m	Green Porosity (vol.%)	Theoretical density (g/cm^3)	Matrix theoretical density (g/cm^3)	Apparent density (g/cm^3)	Real density (g/cm^3)	Total porosity (%)
RII $x=0$	0.15	19 ± 1	3.72	3.82	2.52 ± 0.04	3.60 ± 0.05	30 ± 2
	0.37	21 ± 1	3.67	3.82	n.d.	3.60 ± 0.05	30 ± 1
	0.45	19 ± 1	3.62	3.82	2.40 ± 0.06	3.58 ± 0.05	33 ± 2
RII $x=0.5$	0.15	17 ± 1	3.67	3.84	2.70 ± 0.06	3.65 ± 0.05	26 ± 1
	0.37	21 ± 1	3.66	3.84	2.50 ± 0.02	3.65 ± 0.06	31 ± 2
	0.45	18 ± 1	3.66	3.84	2.50 ± 0.04	3.62 ± 0.05	29 ± 1
RII $x=1$	0.15	20 ± 1	3.72	3.85	2.57 ± 0.04	3.67 ± 0.06	30 ± 1
	0.37	22 ± 1	3.67	3.85	2.52 ± 0.02	3.65 ± 0.06	31 ± 2
	0.45	22 ± 1	3.65	3.85	2.58 ± 0.01	3.68 ± 0.06	30 ± 1
RIII $x=0.5$	0.15	20 ± 1	3.77	3.88	2.72 ± 0.02	3.67 ± 0.06	26 ± 1
	0.37	21 ± 1	3.68	3.88	2.60 ± 0.02	3.66 ± 0.05	29 ± 1
	0.45	20 ± 1	3.66	3.88	2.56 ± 0.01	3.65 ± 0.05	30 ± 1
RIII $x=1$	0.15	15 ± 1	3.74	3.91	2.57 ± 0.04	3.78 ± 0.07	32 ± 1
	0.37	19 ± 1	3.70	3.91	2.52 ± 0.02	3.60 ± 0.05	30 ± 2
	0.45	18 ± 1	3.72	3.91	2.58 ± 0.01	3.58 ± 0.04	28 ± 1

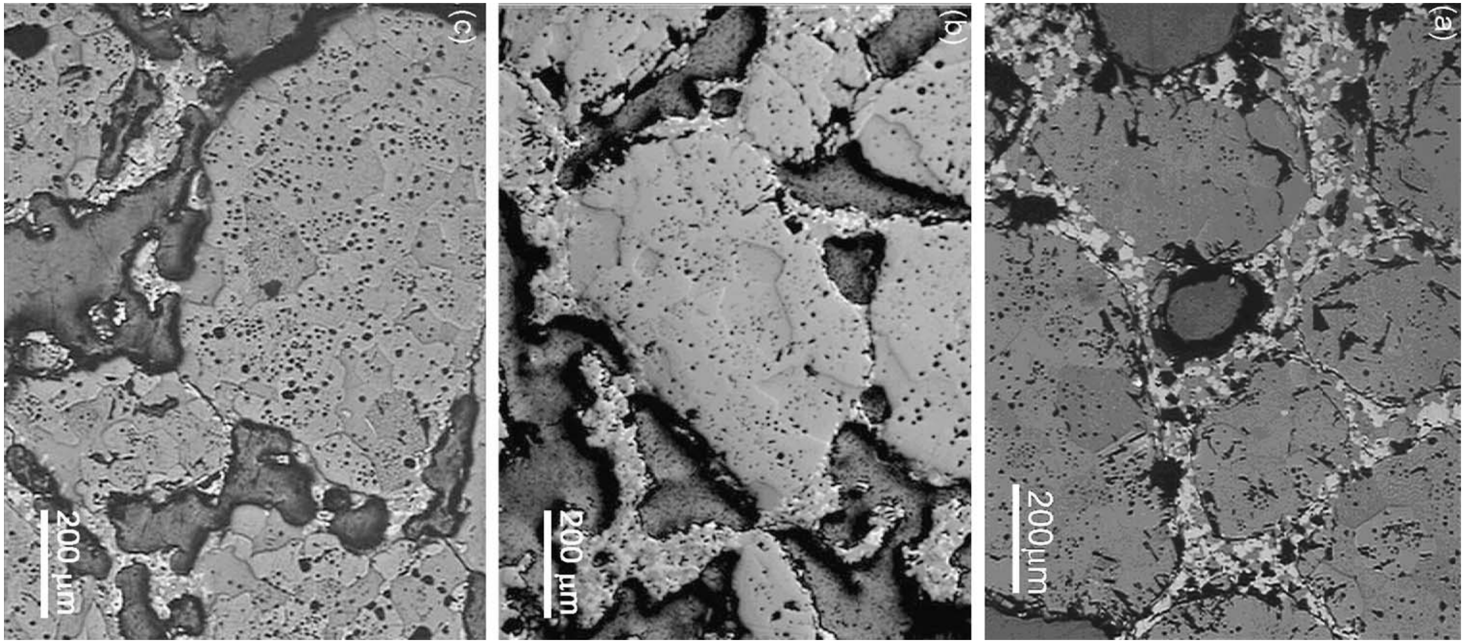

Fig. 2. Characteristic microstructures of the materials RII with $x=0.5$, formulated in the subsystem MgO–$CaZrO_3$–Ca_2SiO_4–$Ca_3Mg(SiO_4)_2$. The large MgO aggregates are the rounded dark gray particles while the presence of different phases in the matrix is revealed by the different colours (identification in Fig. 7). (a)–(c) correspond to materials with decreasing amounts of fines (i.e. increasing module m). Reflected light optical microscopy micrographs of polished surfaces.

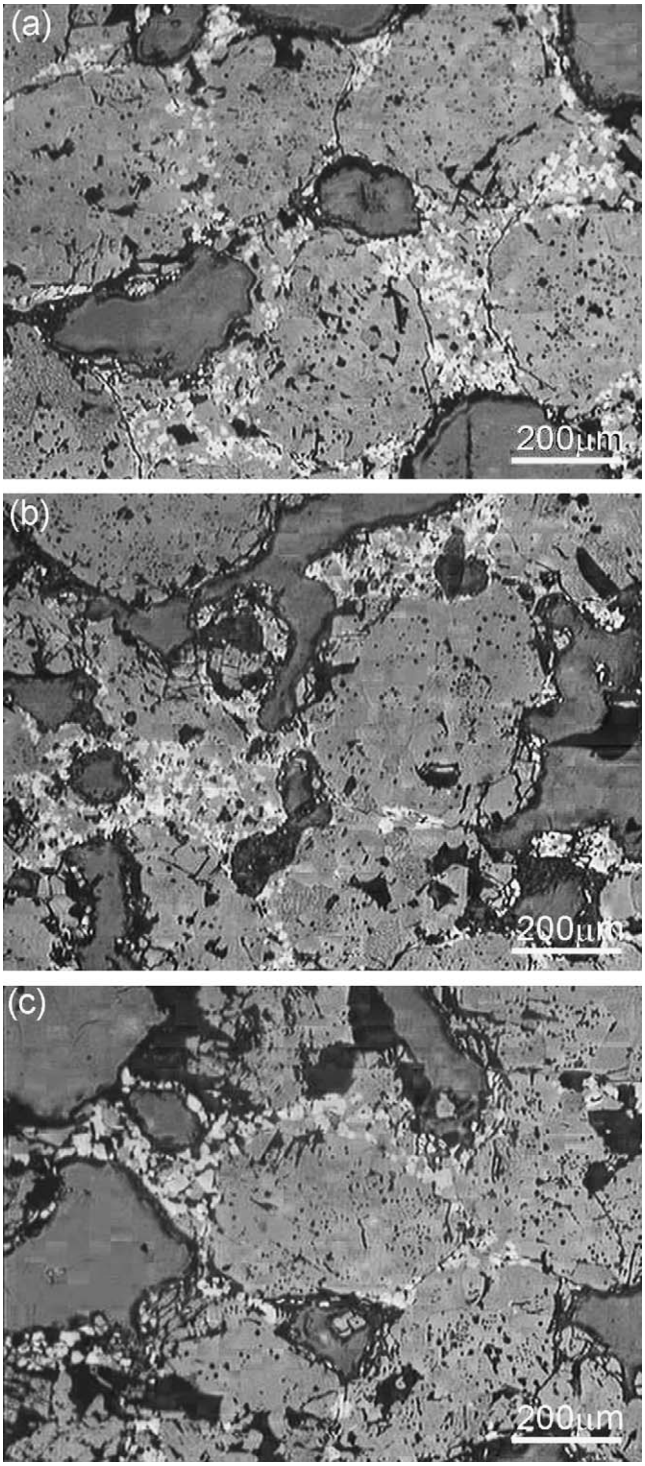

Fig. 3. Characteristic microstructures of the materials RII with $x = 1$, formulated in the subsystem MgO–$CaZrO_3$–$Ca_3Mg(SiO_4)_2$. The large MgO aggregates are the rounded dark gray particles while the presence of different phases in the matrix is revealed by the different colours (identification in Fig. 7). (a)–(c) correspond to materials with decreasing amounts of fines (i.e. increasing module *m*). Reflected light optical microscopy micrographs of polished surfaces.

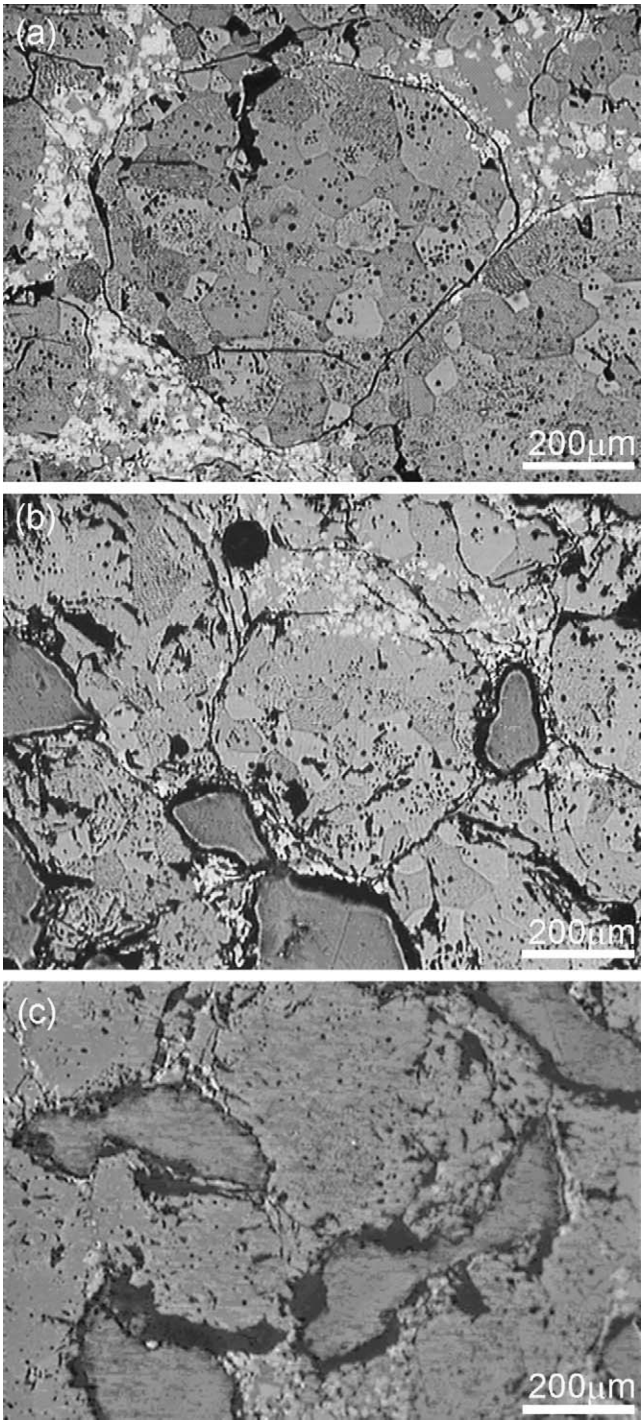

Fig. 4. Characteristic microstructures of the materials RIII with $x = 0.5$, formulated in the subsystem MgO–$CaZrO_3$–ZrO_2–$Ca_3Mg(SiO_4)_2$. The large MgO aggregates are the rounded dark gray particles while the presence of different phases in the matrix is revealed by the different colours (identification in Fig. 8). (a)–(c) correspond to materials with decreasing amounts of fines (i.e. increasing module *m*). Reflected light optical microscopy micrographs of polished surfaces.

ces (<120 μm), formed by the reaction sintering of the initial mixtures of zircon and dolomite, and voids. The aggregates presented porous microstructures with homogeneous grain sizes (∼100 μm) and only small amounts of calcium-rich silicate phases, which can be deleterious to the high temperature prop-

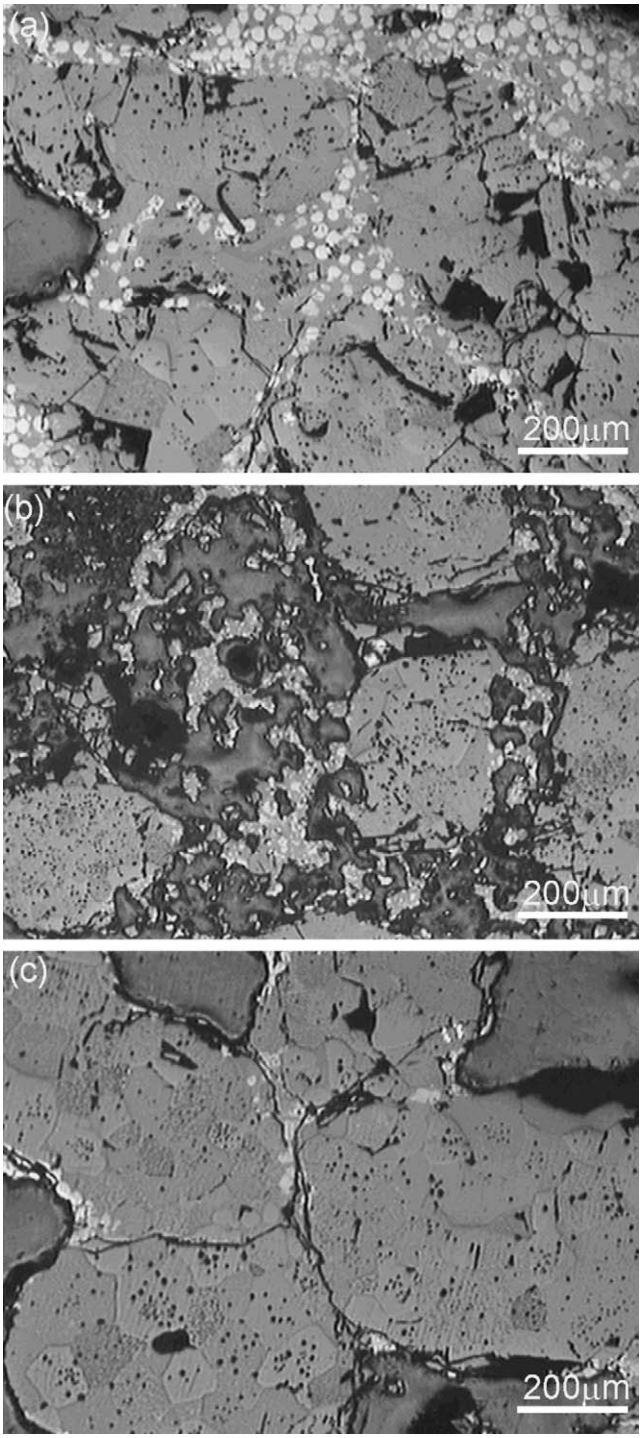

Fig. 5. Characteristic microstructures of the materials RIII with $x = 1$, formulated in the subsystem $MgO–CaZrO_3–ZrO_2$. The large MgO aggregates are the rounded dark gray particles while the presence of different phases in the matrix is revealed by the different colours (identification in Fig. 8). (a)–(c) correspond to materials with decreasing amounts of fines (i.e. increasing module m). Reflected light optical microscopy micrographs of polished surfaces.

erties, in the grain boundaries and triple points. The high proportion of direct MgO–MgO bonding and the absence of B_2O_3 indicated that the aggregates were obtained by calcination at high temperature of a natural cryptocrystalline magnesite.

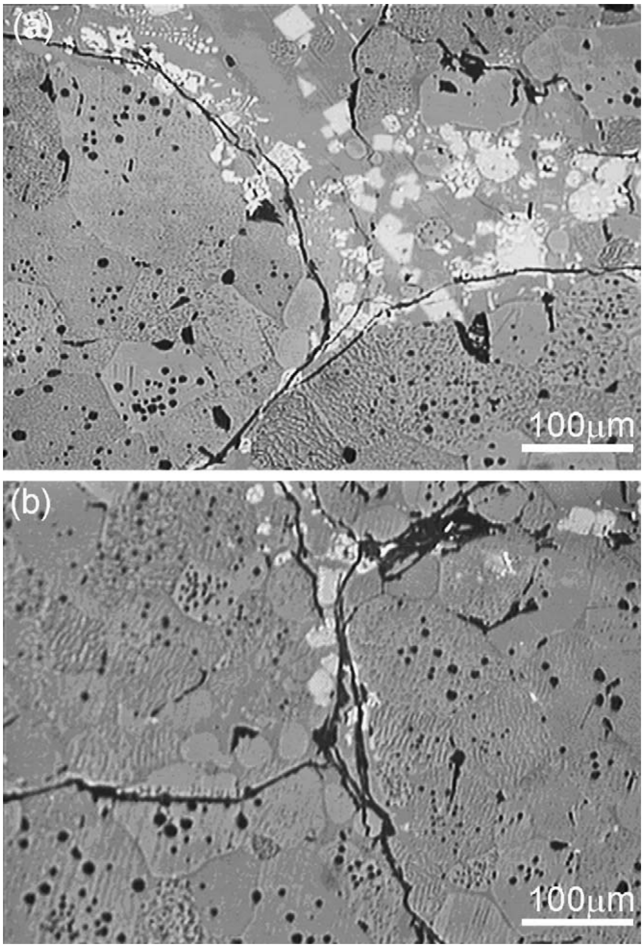

Fig. 6. Characteristic microstructures of sintered samples showing details of the bonding areas between the MgO aggregates and the cracks around them. Reflected light optical microscopy micrographs of polished surfaces. (a) Materials with high matrix proportions: the fine fraction acts as a continuous phase between the agglomerates. RIII $x = 0.5$, $m = 0.15$ specimen sintered at 1500 °C/6 h. (b) Materials with low matrix proportions: direct bonding between the agglomerates is observed. RIII $x = 1$, $m = 0.45$ specimen sintered at 1450 °C/6 h.

A high level of reaction between the matrix and the aggregates was found in materials RIII with $x = 0.5$ and 1 and RII. In materials RII $x = 0.5$ and 1 and RIII $x = 0.5$ this can be explained by the occurrence of reaction sintering in the presence of liquid because the sintering temperatures were about 50 °C higher than the corresponding invariant points (Table 4). In the case of RIII $x = 1$, glassy phase was observed in the microstructure (Fig. 8b) which would indicate that the invariant point for this composition is lower than the sintering temperature for this material (1450 °C, Table 4).

All the studied materials presented similar evolution of the microstructure as a function of the total amount of fines (Figs. 2–5). For the highest amounts (Figs. 2a–6a) the aggregates were surrounded by the matrix that can be considered as the continuous phase whereas a major proportion of contacts between the MgO aggregates was observed for the materials with the lowest amounts of fines (Figs. 2c–5c and 6b). The materials with intermediate amounts of fines (Figs. 2b–5b) presented

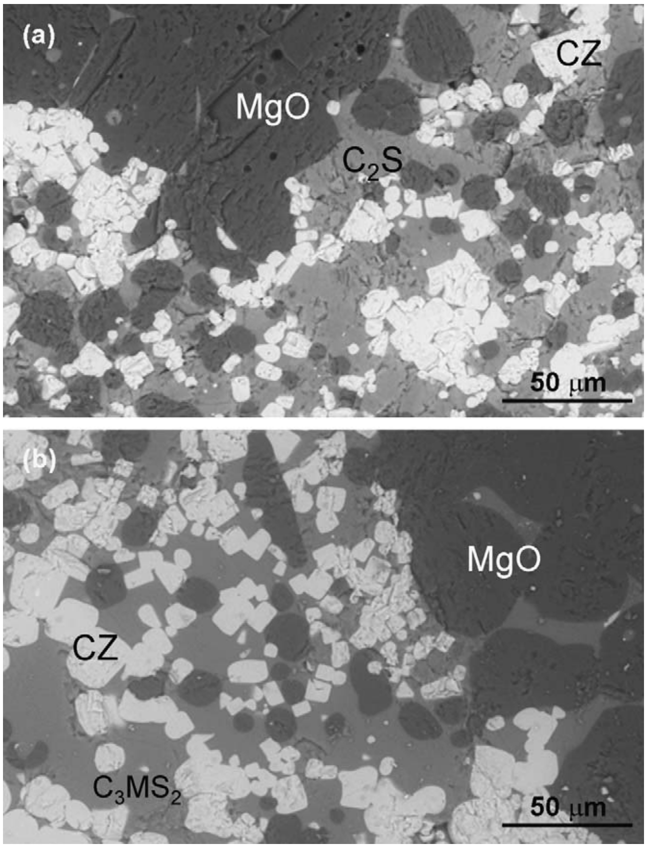

Fig. 7. Characteristic microstructures showing details of the matrices of materials RII. The EDX analyses allowed the identification of the crystalline phases detected by XRD (Table 3). Scanning electron microscope micrographs of polished surfaces. CZ = $CaZrO_3$, C_3MS_2 = $Ca_3Mg(SiO_4)_2$. (a) Materials formulated in the subsystem MgO–$CaZrO_3$–Ca_2SiO_4–$Ca_3Mg(SiO_4)_2$ (RII $x = 0$ and 0.5). (b) Materials formulated in the subsystem MgO–$CaZrO_3$–$Ca_3Mg(SiO_4)_2$ (RII $x = 1$).

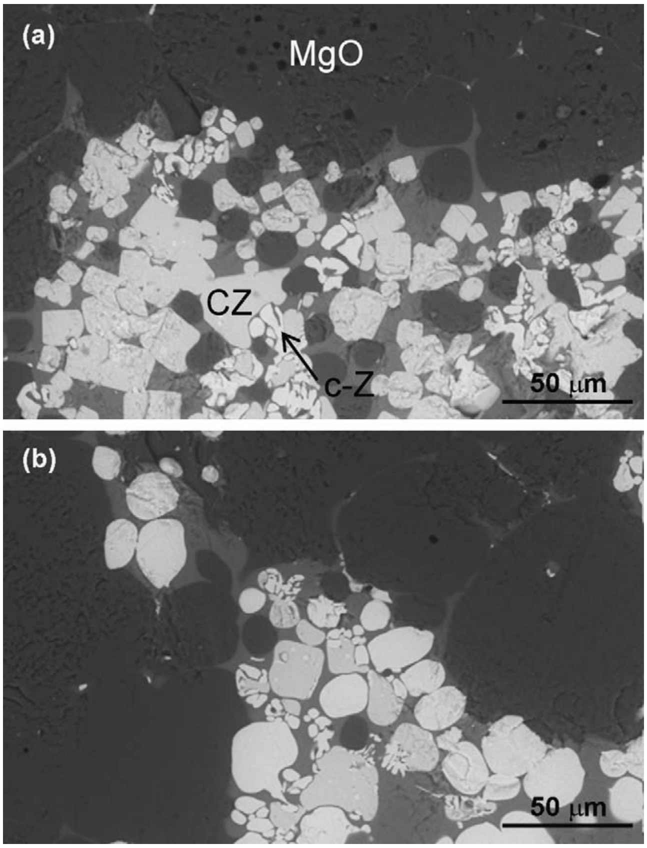

Fig. 8. Characteristic microstructures showing details of the matrices of materials RIII. The EDX analyses allowed the identification of the crystalline phases detected by XRD (Table 3). Scanning electron microscope micrographs of polished surfaces. CZ = $CaZrO_3$, c-Z = cubic ZrO_2. (a) Materials formulated in the subsystem MgO–$CaZrO_3$–ZrO_2–$Ca_3Mg(SiO_4)_2$ (RIII $x = 0$ and 0.5). (b) Materials formulated in the subsystem MgO–$CaZrO_3$–ZrO_2–$Ca_3Mg(SiO_4)_2$ (RIII $x = 1$).

intermediate microstructures with matrix portions between some aggregates and contacts between others.

The crystalline phases detected by XRD could be associated with the different kinds of particles observed by SEM-EDX (Figs. 7 and 8). In all the specimens the large (0.6–3.35 mm) MgO aggregates as well as the smaller (<25 μm) and rounded MgO particles formed during the reaction sintering were observed (Figs. 7 and 8). In the MgO–$CaZrO_3$-additional silicate phase materials (RII compositions, Fig. 7) the matrix was formed by small (<20 μm) $CaZrO_3$ grains surrounded by the calcium silicate phases (Ca_2SiO_4 and $Ca_3Mg(SiO_4)_2$). The microcracking observed in the $CaZrO_3$ grains can be attributed to the high thermal expansion anisotropy of this phase.[16] Microcracking of the $CaZrO_3$ grains formed in the previously studied materials was not detected. Differences are due to the sizes of the $CaZrO_3$ grains formed,[26] small (<2 μm) in solid state reaction sintered materials[14] and large (∼10 μm) in the liquid phase reaction sintered ones studied here (Fig. 7). The high thermal expansion mismatch between the matrix phases (the thermal expansion of β-Ca_2SiO_4 is about twice that of $Ca_3Mg(SiO_4)_2$ and about 60% higher than that of $CaZrO_3$, Table 2), would be partially responsible for the numerous short (≤10 μm) cracks observed through the matrices. Moreover, depending on the grain size, β-Ca_2SiO_4 may transform into γ-Ca_2SiO_4 at about 500 °C during cooling in the RII materials with $x = 0$ and 0.5. This involves a large volume expansion (∼12 vol.%) that would lead to the development of radial cracks emerging from the γ-Ca_2SiO_4 grains. In fact, the material with the highest amount of Ca_2SiO_4 (∼25 vol.%, material RII $x = 0$, $m = 0.15$, Table 5) did not have enough structural integrity to be mechanically tested.

In the c-ZrO_2 containing materials (compositions RIII, Fig. 8) the matrices were constituted by small (<20 μm) c-ZrO_2 and $CaZrO_3$ grains surrounded by a continuous ZrO_2-rich glass. Microcracking of the $CaZrO_3$ grains was less extensive in these materials probably because $CaZrO_3$ was surrounded by glass, a low Young's modulus phase, which can also be responsible for the lack of microcracking due to thermal expansion mismatch between the matrix phases.

In most materials circular cracks at the interfaces between the MgO aggregates and the matrices were observed (Figs. 2–6). These cracks can be explained by the differences between the average thermal expansion coefficients of the matrices and the MgO aggregates. In Table 7 the values are given for the expected average thermal expansion coefficients for the matrices calculated using the properties of the constituent crystalline phases

Table 7
Mechanical properties of the materials and calculated thermal expansion coefficients of the matrices.

Material		Young's modulus (GPa)		Modulus of rupture (MPa)		Work of fracture (J m^{-2})	Calculated α matrix ($\times 10^{-6}$ °C^{-1})
Composition	*m*	Calculated	Experimental	Room temperature	1100 °C		
RII $x=0$	0.15	227	–	–	–	–	13.4
	0.37	241	40 ± 3	2.4 ± 0.3			
	0.45	243	25 ± 3	1.7 ± 0.3			
RII $x=0.5$	0.15	230	67 ± 4	5.2 ± 0.5		60 ± 9	11.0
	0.37	245	39 ± 5	2.4 ± 0.1			
	0.45	249	37 ± 2	2.2 ± 0.3			
RII $x=1$	0.15	227	59 ± 3	3.9 ± 0.1	9 ± 1	40 ± 6	10.2
	0.37	242	48 ± 4	2.9 ± 0.2	7 ± 1		
	0.45	246	80 ± 3	4.5 ± 0.5	15 ± 4	37 ± 3	
RIII $x=0.5$	0.15	227	78 ± 4	6.0 ± 0.5		72 ± 2	9.9
	0.37	241	77 ± 6	4.3 ± 0.1		39 ± 2	
	0.45	245	70 ± 4	4.2 ± 0.2			
RIII $x=1$	0.15	218	60 ± 9	5 ± 1	11 ± 3	55 ± 7	9.4
	0.37	236	37 ± 7	1.7 ± 0.3	5 ± 1		
	0.45	242	69 ± 2	3.7 ± 0.1	10 ± 1	30 ± 1	

(Table 2) and the Turners equation[27]:

$$\alpha = \frac{\sum(\alpha_i K_i F_i/\rho_i)}{\sum(K_i F_i/\rho_i)} \qquad K_i = \frac{E}{3(1-2\nu)} \tag{4}$$

According with Table 7, the matrices of all materials but RII $x=0$ would have lower thermal expansion coefficient ($\alpha \sim 9.5$–11×10^{-6} °C^{-1}) than the MgO aggregates ($\alpha \sim 13.5 \times 10^{-6}$ °C^{-1}), thus residual tensile stresses perpendicular to the MgO–matrix interfaces will develop on cooling from the sintering temperature. Such stresses would lead to the formation of circumferential cracks as observed.

In materials RII $x=0$ the thermal expansion value of the matrix would be similar to that of the MgO aggregates, accordingly, no large and circular cracks were detected in these materials.

3.5. Mechanical characterization

In Table 7 the mechanical properties of the materials are summarised. The calculated Young's module for zero porosity materials were obtained from the values corresponding to each phase (Table 2) and the calculated expected compositions (Table 5) using the Voight limit.[27]

$$E_{\text{calc}} = \sum E_i V_i \tag{5}$$

where E_i and V_i are the Young's modulus and volume fraction for phase *i*, respectively.

As expected for highly porous materials, the experimental Young's modules were much lower than the ones calculated and in the range of those of other MgO refractories.[28]

As shown in Fig. 9, the room temperature bending tests gave always stable or semi-stable fracture, thus, the work of fracture was calculated as the integral under the load–displacement curve divided by the cross section of the specimens. All the curves of tests performed at 1100 °C showed unstable fracture mode.

The values of the room temperature modulus of rupture ranged from 2 to 6 MPa, depending on the material (Table 7); for the same *R* and *x* values they were always the lowest for the intermediate values of the *m* modulus (0.37). The values of the high temperature modulus of rupture were much higher (~200–300%) than those determined at room temperature.

3.6. Relationships between the microstructure and the mechanical behaviour

In order to analyse the relationships between the microstructure of the materials and the mechanical behaviour, the plots of Fig. 10 have been built. In Fig. 10a, the reduced Young's modulus (Experimental *E*/Calculated *E*) versus the final volume fraction of matrix in the sintered materials is plotted. The existence of two families of materials, with the reduced Young's module around 0.15 and 0.3 is apparent. The larger the reduced Young's modulus the closer will be the experimental value to the one expected for materials of the theoretical composition with zero porosity and no cracks. Therefore, it should be possible

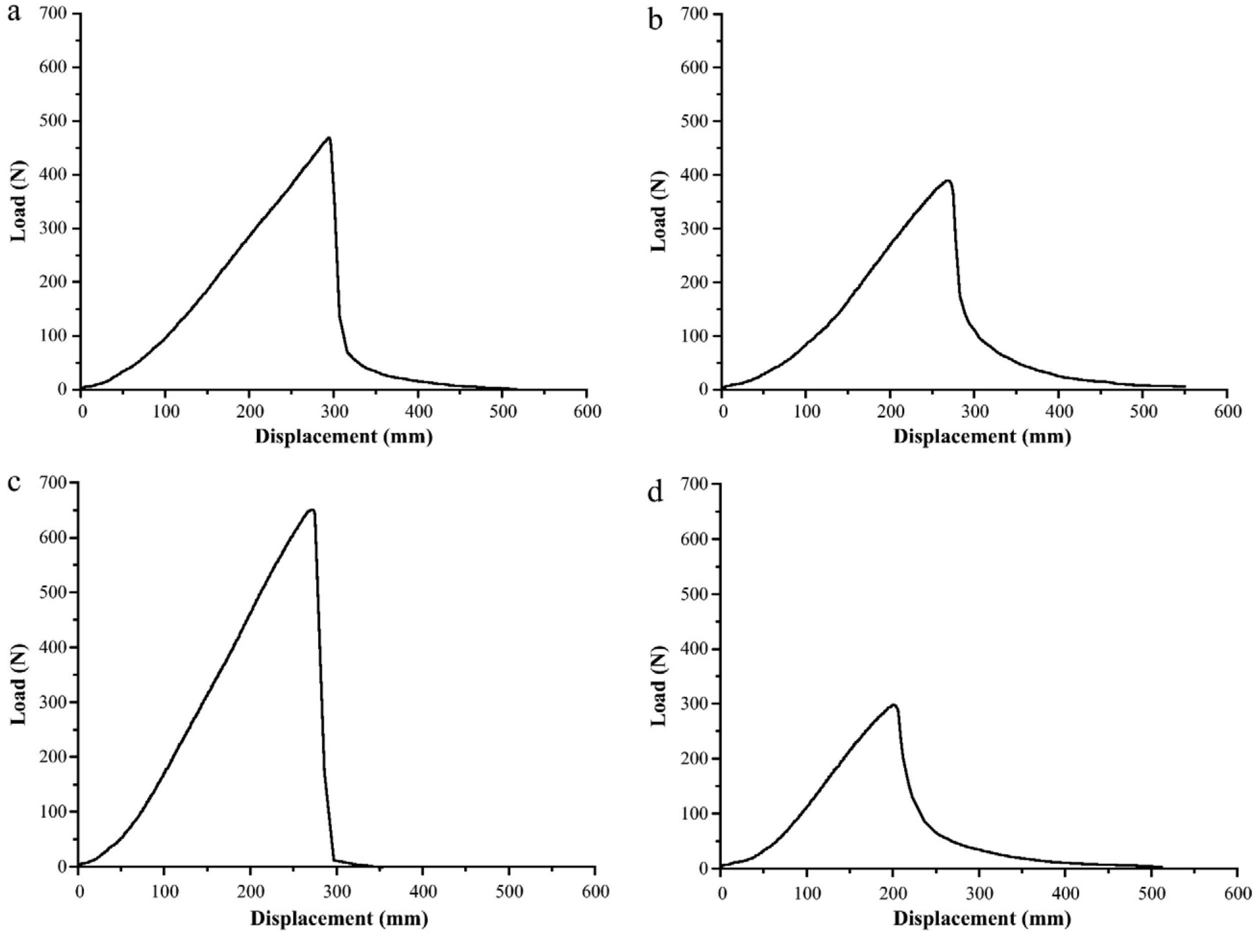

Fig. 9. Characteristic load–displacement curves recorded during the room temperature bending tests. (a) Specimen of material RII $x = 0.5$, $m = 0.15$. Semi-stable fracture is shown. The work of fracture value was 60 J m^{-2}. (b) Specimen of material RII $x = 1$, $m = 0.15$. Stable fracture is shown. The work of fracture value was 46 J m^{-2}. (c) Specimen of material RIII $x = 0.5$, $m = 0.15$. Semi-table fracture is shown. The work of fracture value was 75 J m^{-2}. (d) Specimen of material RIII $x = 1$, $m = 0.15$. Stable fracture is shown. The work of fracture value was 59 J m^{-2}.

to relate the reduced Young's modulus with the microstructural features of the materials.

All materials with large proportions of matrix (>40 vol.%) presented relatively high values of the reduced modulus because in these materials the matrix constituted a continuous bonding between the aggregates (Figs. 2–6a). Part of the materials with low matrix proportions and major proportions of contacts between the MgO aggregates (Figs. 3–5c and 6b) presented also reduced modulus around 0.3. The relationships between the reduced Young's modulus and the matrix volume fractions for these two groups of materials can be rationalised as follows: high reduced modulus are found for materials with high proportions of continuous bonding in their microstructure. For high matrix fractions it is the matrix what plays this bonding role whereas the skeleton formed by the aggregates assures the bond for very low matrix fractions.

There are still five RII and one RIII materials with low matrix fractions that present relatively low reduced Young's modulus, revealing a lack of MgO–MgO bonding. In the case of materials RII this can be related to the high temperatures for liquid formation for these materials as compared to those for the RIII ones which will retard the sintering process. In fact, these materials presented high porosity values (29–31%, Table 6) and large elongated pores along the MgO aggregates (Figs. 3–5c). The RIII material with intermediate amounts of fines and low reduced Young's modulus presented an intermediate microstructure with matrix portions between some aggregates and contacts between others, as observed when comparing its microstructure (Fig. 5b) with those of the other two materials of similar composition (Fig. 5a and c).

In Fig. 10b the room temperature modulus of rupture, MOR, values of the studied materials are plotted versus the square root of the experimental Young's modulus. A fairly good linear relationship is found according to:

$$\frac{\text{MOR}}{(E\,G_c)^{1/2}} = B\,c^{1/2} \qquad (6)$$

where B is a geometrical constant.

Assuming equal values of G_c for the materials studied here, which is reasonable due to the similar low values of fracture toughness of refractories, the linear relationship shown in Fig. 10b would be expected because the large MgO aggregates surrounded by cracks or by a weak microcracked matrix will constitute the critical defects for these materials. From this

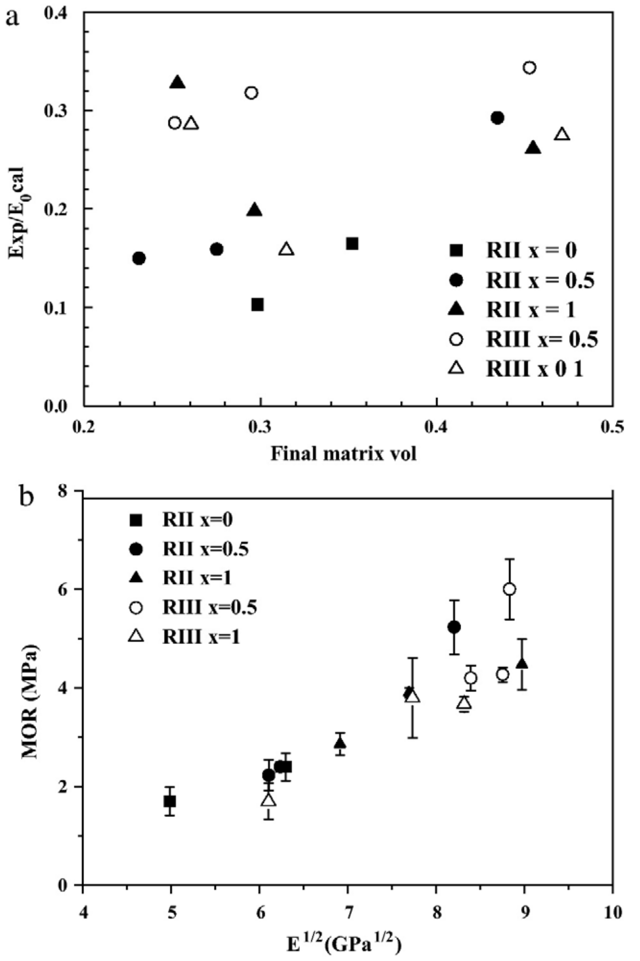

Fig. 10. Representations using the mechanical properties summarised in Table 7 and the matrix proportions from Table 3. (a) Calculated reduced Young's modulus, E_r, versus the final matrix volume fraction. $E_r = E_{exp}/E_0$, E_{exp} = experimental values from Table 7 and E_0 = values calculated from the expected compositions (Table 5) and the properties of the phases (Table 2). (b) Modulus of rupture versus the square root of the experimental Young's modulus to verify relationship from Eq. (6).

result, it can be derived that it would be difficult to try to improve the modulus of rupture for the family of materials studied. Nevertheless values between 4 and 6 MPa can be considered as sufficient for refractories for cement kilns. Moreover, some of the materials with modulus of rupture higher than 4 MPa presented work of fracture values (Table 7) of the same order or higher than those for other oxide refractories (60–90 J m^{-2}).[28]

As in other refractories, the heterogeneous microstructures formed by hard and strong aggregates and weak matrices and/or matrix/aggregate bonds, lead to increased values of work of fracture due to consuming energy phenomena such as microcracking, crack bridging and crack bowing. In fact the highest WOF values were obtained for the materials with the highest values of matrix fractions (Table 7).

The values of the high temperature MOR followed the same dependence on microstructure as the room temperature ones, being the largest for minimum and maximum amounts of fines. The fact that values were much higher than those determined at room temperature (200–300%) can be explained by the decrease of residual stresses and crack closure due to thermal expansion of the different phases as temperature rises.

From the above discussions it is possible to select a group of materials with adequate mechanical properties to be used in cement kilns. In principle, all materials with the highest amounts of fines ($m = 0.15$) and $x = 0.5$ and 1 would have sufficient structural integrity combined with relatively high work of fracture for use in the cement kilns. However, the invariant point corresponding to the compositions of the materials formulated the highest contents of zircon (RIII $x = 1$, final phases $MgO–ZrO_2–Ca_3Mg(SiO_4)_2$) is the lowest (1470 °C, Table 7) and close to that for cement fabrication (1400–1500 °C).[1] Therefore, these materials can only be proposed for the lower and upper transition zones of the kilns. In contrast, the materials with $MgO–CaZrO_3–Ca_2SiO_4–Ca_3Mg(SiO_4)_2$ as final phases (RII $x = 0.5$ and 1), with corresponding invariant point 1550 °C, are adequate to work under the temperature requirements of the burning zones of the cement kilns.

4. Conclusions

Two series of refractory materials have been fabricated from natural dolomite and zircon and with dead burned magnesia aggregates taking into account the phase equilibrium relationships to obtain $MgO–CaZrO_3–Ca_2SiO_4–Ca_3Mg(SiO_4)_2$ or $MgO–CaZrO_3–Ca_3Mg(SiO_4)_2–c-ZrO_2$ as final crystalline phases. The phases present in the materials are those expected from the phase equilibrium relationships in the quaternary system.

The optimum microstructures, i.e. minimum porosity and adequate matrix content to constitute the bonding between the aggregates are found for initial matrix fractions higher than those for non-reactive systems.

A series of materials with adequate properties to be used in cement kilns fabricated from dolomite and zircon have been developed. For optimum starting mixtures, materials with Young's modulus (60–80 GPa), modulus of rupture (4–6 and ~10 MPa at 25 and 1100 °C, respectively) and work of fracture (40–70 J m^{-2}) values in the range of those of other magnesia-based refractories have been obtained. For zircon amounts in the starting matrices between 29 and 35 wt.% the obtained materials are adequate to be used in the burning zones of the cement kilns whereas for zircon contents between 35 and 41 wt.% the obtained materials are suitable for use at temperatures up to 1400 °C.

Acknowledgements

This work was supported by MICIN (Spain) under the projects MAT2006-13480-C02 and MAT2006-12749-C02-01, and by project FOMIX COAH-2003-C02-03 (Mexico). Álvaro Obregón wishes to acknowledge financial support of CONACYT (Mexico).

References

1. Feytis A. Between the linings. *Ind Miner* 2010;**6**:46–51.
2. Lee WE, Moore RE. Evolution of in-situ refractories in the 20th century. *J Am Ceram Soc* 1998;**81**(6):1385–410.

3. Bray DJ. Toxicity of chromium compounds formed in refractories. *Am Ceram Soc Bull* 1985;**64**(7):1012–6.
4. White J. Recent applications of phase diagrams to problems in the field of refractory materials. In: Alper A, editor. *Phase diagrams*, vol. IV. New York: Academic Press; 1976. p. 233–97.
5. Pena P, Vázquez B, Caballero A, De Aza S. Diagramas de equilibrio de fases cuaternarios. Métodos de representación e interpretación. *Bol Soc Esp Ceram V* 2005;**44**(2):113–22.
6. Sircar A, Brett NH, White J. Phase Studies in the system CaO–MgO–ZrO_2–SiO_2. Part II: Compatibility relations of zirconia. *J Trans Br Ceram Soc* 1978;**77**(3):77–88.
7. Serena S, Sainz MA, Caballero A. Corrosion behavior of MgO/$CaZrO_3$ refractory matrix by clinker. *J Eur Ceram Soc* 2004;**24**(8):2399–406.
8. Rodríguez-Galicia JL, De Aza AH, Rendón-Ángeles JC, Pena P. The Mechanism of corrosion of MgO–$CaZrO_3$–calcium silicate materials by cement clinker. *J Eur Ceram Soc* 2007;**27**(1):79–89.
9. Serena S, Sainz MA, Caballero A. The system clinker–MgO–$CaZrO_3$ and its application to the corrosion behavior of $CaZrO_3$/MgO refractory matrix by clinker. *J Eur Ceram Soc* 2009;**29**(11):2199–209.
10. Guo Z, Palco S, Rigaud M. Bonding of cement clinker onto doloma-based refractories. *J Am Ceram Soc* 2005;**88**(6):1481–7.
11. Rodríguez JL, Pena P. Obtención de materiales de magnesia-circonato dicálcico por sinterización reactiva de mezclas dolomita – circón. Estudio del procesamiento. *Bol Soc Esp Ceram V* 2001;**40**(6):463–71.
12. Rodríguez JL, Rodríguez MA, De Aza S, Pena P. Reaction sintering of zircon–dolomite mixtures. *J Eur Ceram Soc* 2001;**21**(3):343–54.
13. Rodríguez JL, De Aza S, Pena P. Effect of agglomerate and grain size on the reaction sintering of zircon–dolomite mixtures. *Brit Ceram Trans* 2001;**100**(4):181–91.
14. Rodríguez JL, Baudín C, Pena P. Relationships between phase constitution and mechanical behaviour in MgO–$CaZrO_3$–calcium silicate materials. *J Eur Ceram Soc* 2004;**24**(4):669–79.
15. Rodríguez-Galicia JL, Fernandez-Arguijo B, Rendón-Ángeles JC, Valle FJ, Pena P. Reaction sintering of mexican dolomite–zircon mixtures. *Bol Soc Esp Ceram V* 2005;**44**(3):185–91.
16. Mathews MD, Mirza EB, Momin AC. High temperature X-ray diffractometric studies of $CaZrO_3$, $SrZrO_3$ and $BaZrO_3$. *J Mater Sci Lett* 1991;**10**:305–6.
17. Lee WE, Rainforth WM. Refractory materials. In: *Ceramic microstructures: property control by processing*. London, UK: Chapman & Hall; 1994. p. 470–88.
18. Richerson DW. *Modern ceramic engineering, properties, processing and use in design*. 2nd ed. rev. and expanded New York: Publ. Marcel Dekker, Inc.; 1992 (Chapter 4, p. 150).
19. Hou TI, Kriven WM. Mechanical properties and microstructure of Ca_2SiO_4–$CaZrO_3$ composites. *J Am Ceram Soc* 1994;**77**(1):65–72.
20. Donzel L, Roberts GS. Microstructure and mechanical properties of cubic zirconia (8YSZ)/SiC nanocomposites. *J Eur Ceram Soc* 2000;**20**(14–15):2457–62.
21. Taylor D. Thermal expansion data. VII. Complex oxides AB_2O_4. *Brit Ceram Trans J* 1985;**84**(5):149–53.
22. Abraham I, Gritzner G. Mechanical properties of doped zirconia cubic ceramics. *J Mater Sci Lett* 1993;**12**:995–7.
23. Funk JE, Dinger DR. Particle size control for high-solids castable refractories. *Am Ceram Soc Bull* 1994;**73**:66–9.
24. Alvarez C, Criado E, Baudín C, Duphia G, Kelichaus H. Hot modulus of rupture automatic testing machine. In: *Proceedings of the UNITECR '93 Congress*. Sao Paulo, Brazil: Asociación Latinoamericana de Fabricantes de Refractarios; 1993. p. 435–41.
25. De Aza AH, Rodríguez MA, De Aza S, Pena P, Turrillas X. The decomposition of dolomite monitored by neutron thermodifractometry. *J Am Ceram Soc* 2002;**85**:881–8.
26. Moya JS, Pena P, De Aza S. Transformation toughening in composites containing dicalcium silicate. *J Am Ceram Soc* 1985;**68**(91):C-259–62.
27. Kingery WD, Bowen HK, Uhlmann DR. *Introduction to ceramics*. USA: Ed. A. Wiley-Interscience, Publication John Wiley & Sons; 1979.
28. Baudín C. High temperature mechanical behavior of magnesia–graphite based refractories. In: *Fundamentals of refractory technology, ceramic transactions, vol. 125.* Westerville, OH: Ed. James P. Bennett and Jeffery D. Smith. The Am. Ceram. Soc.; 2001. p. 73–92.